
# Facilitated proton transfer across liquid|liquid interfaces under forced hydrodynamic conditions. Determination of partition coefficients of neutral weak bases

F. Vega Mercado, J.M. Ovejero, F.M. Zanotto, M.R. Serial, M.I. Velasco, R.A. Fernández, R.H. Acosta, S.A. Dassie

PII: S1572-6657(17)30154-6
DOI: doi: 10.1016/j.jelechem.2017.03.005
Reference: JEAC 3170

To appear in: *Journal of Electroanalytical Chemistry*

Received date: 28 December 2016
Revised date: 15 February 2017
Accepted date: 2 March 2017

Please cite this article as: F. Vega Mercado, J.M. Ovejero, F.M. Zanotto, M.R. Serial, M.I. Velasco, R.A. Fernández, R.H. Acosta, S.A. Dassie , Facilitated proton transfer across liquid|liquid interfaces under forced hydrodynamic conditions. Determination of partition coefficients of neutral weak bases. The address for the corresponding author was captured as affiliation for all authors. Please check if appropriate. Jeac(2017), doi: 10.1016/j.jelechem.2017.03.005

# Facilitated proton transfer across liquid|liquid interfaces under forced hydrodynamic conditions. Determination of partition coefficients of neutral weak bases.

F. Vega Mercado[1], J.M. Ovejero[1], F.M. Zanotto[1], M.R. Serial[2], M.I. Velasco[2], R.A. Fernández[1], R. H. Acosta[2], S.A. Dassie[*,1]

[1]Instituto de Investigaciones en Fisicoquímica de Córdoba (INFIQC) - CONICET, Departamento de Fisicoquímica, Facultad de Ciencias Químicas, Universidad Nacional de Córdoba, X5000HUA, Ciudad Universitaria, Córdoba, Argentina.

[2]FaMAF-Universidad Nacional de Córdoba and IFEG-CONICET, X5000HUA, Ciudad Universitaria, Córdoba, Argentina.

**Abstract:**

A novel quantitative methodology to determine the partition coefficients of neutral weak bases is developed. This new electrochemical approach is based on the measurement of the total transferred charge across the oil|water interface under forced hydrodynamic conditions. The complete procedure has been validated by computational simulations and experimental results (Tylosin A). In addition, flow pattern caused inside the electrochemical cell were simulated with computational fluid dynamics using finite element methods and correlated with experimental results obtained by magnetic resonance imaging.

**Keywords:** Finite element method, partition coefficient, facilitated proton transfer, liquid|liquid interface, forced hydrodynamic conditions, Magnetic Resonance Imaging.

*Corresponding author: TE/FAX: ++54-351-4334188.

*e-mail address*: sdassie@fcq.unc.edu.ar (S.A. Dassie)

## 1. Introduction

The transfer of weak acids and bases across liquid|liquid interfaces is reported in several experimental works [1–33]. The transfer processes of protonated species present a strong dependence on the pH of the aqueous phase and on their partition coefficient. The theoretical approximation for the processes of facilitated transfer of protons or the transfer of protonated species has aroused great interest in the area [12,16]. Dassie and co-workers [24,28,33–35] have developed the general equations for a model of ion transfer reactions across the oil|water interface assisted by a neutral weak base. Those analyses were centred mainly on the effect of water autoprotolysis on the transfer processes of the protonated species [34]. The model was corroborated by experimental results obtained from the transfer of quinine across the $H_2O$|1,2-dichloroethane interface, and the corresponding transfer mechanism was analysed in terms of the current-potential and theoretical concentration profiles [24,28,33]. In recent papers, we developed the models for the facilitated proton transfer or charged species transfer across liquid|liquid interfaces including ion pairing [31,32] and non-ideal electrolyte solutions [32] to calculate the half-wave potential for neutral weak bases [31] and weak acids [32].

The electrochemical study of ion transfer at the interface between two immiscible electrolyte solutions (ITIES) has allowed the determination of relevant thermodynamic and transport parameters, provided that the processes measured are limited by mass diffusion. For the study of kinetic parameters and mechanistic information, different experimental approaches have been employed in order to obtain a high mass-transport rate [36–42]. The imposition of a convective flow to increase the mass-transport has also been reported [43–57]. Recently, Dryfe and co-workers [29] presented a novel method, which employed an

organic membrane fitted on the liquid|liquid interface and therefore, it allowed rotation of the produce interface, for the determination of the diffusion coefficient of weakly ionised species [30].

On the other hand, forced hydrodynamic conditions (FHCs) imposed during the potential sweep have been employed to elucidate ion transfer mechanisms in a new methodology proposed by Dassie and co-workers [58]. In this experimental setup, the convective flow in one phase cause an asymmetry of the diffusion field, that is, a selective decrease in the diffusion layer thickness is generated on one side of the interface. This allows to distinguish the direction of the ion transfer [27,59,60]. Recently, we presented the general equations for a model that describes ion transfer reactions across the oil|water interface assisted by a neutral ligand, under FHCs. The model was solved numerically using explicit finite difference and the results of numerical simulations were obtained for simple and facilitated ion transfer [61]. As expected, the flow pattern in the experimental setup plays an important role over the mass transport phenomena within the ITIES cell. Several techniques allow the experimental study of the fluid dynamics in complex systems like a RDE cell. Magnetic resonance imaging (MRI) stands as a suitable tool for this purpose, since it is non-invasive and non-destructive [62–65]. One of the main advantages of the technique resides in the fact that a spin bearing nuclei, in general $^{1}H$, which is part of the flowing liquid, is used to determine the flow patterns, so tracer particles are not needed. This has two benefits, on one hand the flow is not disturbed by impurities, and on the other hand any liquid, even non-transparent liquids can be used, in opposition to optical methods. Moreover, in the study of multi-phase systems, the differences in magnetic relaxation time may be used as a contrast agent; allowing the study of individual components dynamics with the proper experimental parameters [66–68].

In the recent past, different electrochemical approaches for the determination of the partition coefficient of neutral weak bases were applied. In particular, $\Delta_o^w\phi_{1/2,HB^+}$ [6,14,22,69] and $I_{peak}$ [25] are commonly used to calculate the partition coefficient. In the first case, the determination is based on the direct measurement of the voltammetric half-wave potential, which can be directly related to the standard transfer potential [6,69]. This method is valid only for the transfer of a neutral weak base whose concentration in the organic phase are negligible. On the other hand, Senda and co-workers [14,22] used reversible half-wave potential vs. pH curves to determine the standard transfer potential of ions at an oil|water interface based on voltammetric measurements. In this work, the partition processes of both protonated and neutral forms of the organic bases are taken into account. The partition coefficients of neutral and ionic forms of organic bases are determined from the reversible half-wave potential. Finally, Dassie and co-workers examine the variation of peak current values vs. pH or volume ratio curves to determine the partition coefficient of neutral weak bases at an oil|water interface based on voltammetric measurements, considering all the acid-base equilibria and the partition processes of both protonated and neutral forms [25].

In this work an alternative quantitative methodology for the determination of the partition coefficient of neutral weak bases is developed. This new electrochemical approach is based on the measurement of the total transferred charge across the oil|water interface under FHCs. The complete procedure has been validated by computational simulations and experimental results for monoprotic species. In addition, flow pattern caused inside the electrochemical cell were simulated with computational fluid dynamics (CFD) using finite element methods (FEM) and correlated with experimental results obtained by MRI.

**Table 1: Parameters using in this work**

| Symbol | Definition | Unit |
|---|---|---|
| $V_o$ | Organic phase volume | L |
| $V_w$ | Aqueous phase volume | L |
| $r = V_o V_w^{-1}$ | Volume ratio | - |
| $K_{D,B}$ | Partition coefficient of the neutral species B | - |
| $K^{\alpha}_{a,HB^+}$ | Acid dissociation constant in the α-phase | - |
| $v_x^{\alpha}$ | Monodimensional convection velocity in the α-phase | $m\,s^{-1}$ |
| $q^{v_x^{\alpha}}$ | Total charge obtained under FHC's applied to the α-phase | C |
| $q^{v_x^{\alpha}=0}$ | Total charge obtained for quiescent solutions | C |
| $c_B^{init}$ | Initial concentration of the weak base | $mol\,L^{-1}$ |
| $a$ | Linear regression slope | - |
| $v$ | Potential sweep rate | $V\,s^{-1}$ |
| $\mathbf{u}$ | Fluid velocity field | $m\,s^{-1}$ |
| $\omega$ | Angular velocity of rotating rod | $s^{-1}$ |
| $B_0$ | Magnetic field | Tesla |
| $\boldsymbol{G}$ | Magnetic field gradient | $Tesla\,m^{-1}$ |
| $G_{vel}$ | Magnetic field gradient intensity | $Tesla\,m^{-1}$ |
| $\boldsymbol{r}$ | Position vector | m |
| $\gamma$ | Nuclear gyromagnetic ratio | $Hz\,Tesla^{-1}$ |
| $\delta$ | Magnetic field gradient pulse duration | s |
| $\Delta$ | Delay between magnetic field gradient pulses | s |
| $\boldsymbol{v}$ | Stationary velocity of nuclei | $m\,s^{-1}$ |

### 1.1. Theory

The one-dimensional model used to develop the proposed methodology is a revised and extended version of the model proposed by Ovejero et al. [61] and it is described in detail in the Supplementary Material (Section A1 and A2).

The one-dimensional model is used basically as a proof-of-concept. One-dimensional convection velocity is a naive approach to represent the fluid velocity field inside the electrochemical cell. This model is very simple to apply, easy to analyze, and computationally inexpensive; and allows us to understand the general behavior of the system. Furthermore, in the model proposed here, it is assumed that convection velocity is independent of the distance from the interface. A simple model that is commonly used for rotating disk electrodes was proposed by Cochran and Levich [70,71]. It takes into account a disk of infinite diameter in contact with a solution of infinite depth. In contrast, in this case the real dimensions and shape of the cell directly affect the fluid velocity field [72,65]. In the case of the electrochemical cell used in this work, the liquid|liquid interface is generated in a drill-hole (diameter of 4.8 mm) in a glass plate (2 mm thick). The fluid is propelled outwards in the radial direction by the spinning rod, and as it reaches the external walls, it must change direction. This defines different recirculation regions both at the rod's side and below it [72,65]. These regions extend well beyond the vicinity of the disk and allow for the fluid to move downwards along the walls of the electrochemical cell and reach the hole in the glass plate presenting normal velocity components (axial velocities) directed towards the interface. At the center of the cell, the fluid is pulled upwards by the movement of the rod. In this way, chemical species are carried towards and from the vicinity of the interface. This complex behavior of the fluid near the liquid|liquid interface is represented by a "convection velocity" parameter in the one-dimensional model.

Subsequently, this approach was validated with results obtained by FEM simulations appropriated of greater complexity.

## 2. Materials and methods

### 2.1. Electrochemical setup

The electrochemical experiments were performed in a four-electrode system using a conventional glass cell of 0.18 $cm^2$ interfacial area. Two platinum wires were used as counter-electrodes; the reference electrodes were Ag|AgCl|$Cl^-$. The reference electrode in contact with the organic solution was immersed in an aqueous solution of 1.0 x $10^{-2}$ M tetraphenylarsonium chloride (TPACl) (Merck p.a.). The potential values reported (*E*) are the potentials applied including $\Delta_o^w\phi_{tr,\mathrm{TPA}^+}^{o'} = -0.364\,\mathrm{V}$ for the transfer of the reference ion $TPA^+$. The supporting electrolytes are $1.0\,\mathrm{x}10^{-2}\,\mathrm{M}$ KCl (J.T. Baker p.a.), in ultrapure water, and $1.0\,\mathrm{x}10^{-2}\,\mathrm{M}$ tetraphenylarsonium dicarbollylcobaltate (TPADCC) in 1,2-dichloroethane, 1,2-DCE, (Dorwil p.a.). TPADCC was prepared as described in ref. [73]. Tylosin A tartrate (Sigma) was used without further purification and was always dissolved in the aqueous phase. The pH values were adjusted using phosphate or acetate as a buffer. Three different pH values were chosen as reference depending on the system in different sections. S1 correspond to pH value where transfer mechanism denoted by reaction (I) prevail (generally pH=2.0); S2 correspond to pH value where transfer mechanism denoted by reaction (II) prevail (pH=6.8 or 8.0) and S3 correspond to an intermediate pH (generally pH=4.5 or 5.0).

All the voltammograms shown in this work correspond to solutions in acid-base and partition equilibria. Aqueous and organic phases were equilibrated stirring different

amounts of each phase in contact (initial system). This was performed in a stoppered flask for 1 hour. The volume ratio *r* is defined as the ratio between the organic phase volume ($V_o$) and the aqueous phase volume ($V_w$). The electrochemical cell was composed by two solutions in equilibrium with the same properties as the initial system [24,25,27,28,60].

Cyclic voltammetry was carried out using a potentiostat which automatically eliminated the *iR* drop by means of a periodic current-interruption technique [74]. FHCs were applied with a polytetrafluoroethylene (PTFE) cylinder (analogue to a rotating-disc electrode) controlled by a PINE disc rotator [58].

All experiments were repeated at least three times and showed to be reproducible with dispersion in the charge values lower than 5%.

### 2.2. Magnetic Resonance Imaging

The aim of this section is to provide a simplified overview of the basic elements involved in nuclear magnetic resonance imaging (MRI). For detailed descriptions of the method, see Ref. [75] and specific applications in electrochemistry in Refs. [63,76–79]. NMR is based on the fact that nuclear spins undergo a precession around the direction of the magnetic field induced by an external magnet ($B_0$). In MRI an extra set of magnetic fields that change linearly with space are used. These magnetic field gradients ($\boldsymbol{G}$) give rise to a frequency that depends on the position ($\boldsymbol{r}$) as:

$$\omega_0(\boldsymbol{r}) = \gamma(B_0 + \boldsymbol{r}\cdot\boldsymbol{G}) \quad (1)$$

where $\gamma$ is the nuclear gyromagnetic ratio of the observed isotope (e.g. $^{1}$H, $^{19}$F, $^{7}$Li). A Fast Fourier Transform (FFT) of the signal decay renders a projection of the object in the

direction where the gradient is applied; this is usually referred to as a 1D image. In order to obtain a 3D image of an object, a set of three orthogonal gradients are used to encode the position of spins in each direction.

### 2.3. Velocity maps

If the spin bearing molecules are moving along *z* during the application of a magnetic field gradient of duration $\delta$, an extra accumulation in the phases will be produced as [80]:

$$\phi = \int_0^{\delta} \gamma G_{\text{vel}}(t) z(t) dt \tag{2}$$

In this work a pair of bipolar gradients was applied in order to impart a phase proportional to the displacement of the sample in the direction in which the gradients are applied. This phase depends on the gradient intensity ($G_{\text{vel}}$), the pulse time duration ($\delta$) and the spacing between them ($\Delta$).

If nuclei are moving with a stationary velocity, $\boldsymbol{v}$, in an arbitrary direction, the net phase for bipolar gradients can be written as:

$$\phi = \gamma \delta \Delta \boldsymbol{G}_{\text{vel}} \cdot \boldsymbol{v} \tag{3}$$

Velocity maps in a given spatial direction are obtained by calculating the phase difference between a reference image measured without velocity gradients and a second image measured with the bipolar gradient pair applied along the desired spatial direction [75]. The phase of the signal of both images is subtracted and the pixel by pixel phase difference is converted to velocities using Eq. (3), where the velocity of the nuclei contained in a volume element, or voxel, is considered to be stationary.

### 2.4. MRI setup

All experiments were carried out at 7.05 Tesla ($\nu_0 = 300.13$ MHz) in an Oxford superconducting magnet operated with a Kea2 (Magritek GmbH) console. A 3D gradient coil system (Bruker GmbH) with maximum gradients of 1.5 Tesla $m^{-1}$ was used. Radiofrequency excitation and detection was carried out with a 25 mm inner diameter Bruker GmbH birdcage coil with a length of 37 mm. A hard 90º pulse of 250 µs and a 180º Gaussian selective pulse of 700 µs of duration were used.

A simplified electrochemical cell was built in glass, with a rotating cylinder analogous to the RDE made from polyacetal resin. The lower part of the container was filled with 1,2-dichloroethane and the upper part with deionized water. The rotation speed of the cylinder was 62.8 $s^{-1}$.

The 3D velocity map was acquired from two 3D images, one reference without velocity gradient and one image with velocity gradient applied in the *z* direction. The field of view was set to (40 × 20 × 20) $mm^3$ in the *z*, *x* and *y* directions. Matrices of 128 × 32 × 32 points were acquired, giving rise to a resolution of (0.313 × 0.625 × 0.625) $mm^3$. The most relevant parameters of the pulse sequence were the following: echo time: $t_E$ = 14ms, $\delta$ = 1.0 ms and $\Delta$ = 2.2 ms. In all the cases, the dwell time was 5µs and the acquisition time was 0.64 ms. The total experimental time was approximately 17 min, in which 2 acquisitions were acquired and averaged. A waiting period of ten minutes was introduced between the startup of the rotations until the acquisition of the images. All experiments were repeated at least three times and showed to be reproducible with dispersion in the velocity values of 5%.

## 3. Results and discussion

In general, it is possible to postulate a transfer mechanism for protonatable neutral weak bases consisting in two different processes [25,31]: a general transfer reaction (transfer of $HB^+$ previously formed in the aqueous phase):

$$HB^+(w) \rightleftharpoons HB^+(o) \quad \text{(I)}$$

and a facilitated proton transfer by interfacial protonation that depends on the $K_{D,B}$ values:

if $K_{D,B} > 1$

$$H^+(w) + B(o) \rightleftharpoons HB^+(o) \quad \text{(II)}$$

if $K_{D,B} < 1$

$$H^+(w) + B(w) \rightleftharpoons HB^+(o) \quad \text{(III)}$$

and, if $K_{D,B} \approx 1$, the reactions (II) and (III) take place simultaneously in different proportions. These proposed mechanisms for each case, represent the limiting behaviours of a unique transfer reaction because the aqueous phase is bufferized. But, it should be noted that global reactions (II) and (III) involve higher energies of the ion transfer than the direct transfer (reaction (I)).

### 3.1. Novel approach to the determination of the partition coefficient of the neutral weak bases

In this section, we propose a novel electrochemical approach for the determination of the partition coefficient of neutral weak bases based on the measurement of the charge values when FHCs are applied in the organic or in the aqueous phase. This electrochemical approach is developed using the one-dimensional model. Obviously, the total transferred charge, $q$, in the forward potential sweep is directly related to the total amount of matter

transferred and related to the transfer mechanism. The total amount transferred is dependent of thermodynamic parameters, including acid-base dissociation constants in both phases and partition coefficient. The amount of matter transferred can also be modulated by experimental conditions such as volume ratio, pH, initial concentration of the weak base, cylinder rotation speed or convection velocity, and sweep rate. Thus, the complete analysis and control of these experimental conditions were properly handled for the determination of the partition coefficient.

Fig. 1a shows the behaviour of the total transferred charge in the forward potential sweep as function of pH when both phases are in quiescent conditions and when FHCs are applied for a hydrophobic weak base. It is worth pointing out that when both phases are in quiescent conditions, as pH increases, the transfer mechanism changes from reaction (I) to reaction (II), and, since $r<1$ and the neutral weak base is hydrophobic, a preconcentration effect of the organic neutral species occurs; therefore $q$ is greater when the reaction (II) is predominant. Now, if FHCs are applied to the organic phase, the total charge values are the same in both stirred and an unstirred conditions at low pH values. This is a clear indication that the transfer process is controlled by the diffusion of the species ($HB^+$) present in the unstirred aqueous phase. However, at high pH values, the total charge increases dramatically with FHCs applied to the organic phase. This is because under these experimental conditions mass transport is controlled by the neutral base, B, present in the organic phase (reaction (II)), and the aqueous phase is a buffer solution. On the other hand, when the aqueous phase is stirred at low pH values, $q$ is higher than the unstirred process because the transferring species is initially in the aqueous phase and a stationary current in the forward sweep is observed in the respective voltammogram. At higher pH values, the

total charge decreases reaching the same values of the unstirred situation, indicating the prevalence of the facilitated proton transfer mechanism (reaction (II)), for which the limiting species is initially in the non-stirred phase.

Another key parameter that affects the total transferred charge is the fluid velocity, which in this case is denoted by the convection velocity, $v_x^{\alpha}$. Fig 1b shows the total transferred charge as a function of $v_x^{\alpha}$ obtained at three different pH values (pH 2.0 S1, pH 5.0 S3 and pH 8.0 S2) and for FHCs in aqueous or organic phases. This figure shows that the total charge increases as the convection velocity increases due to an increment in the mass transport rate.

**3.2. Description of the methodology based on FHCs varying stirring frequency**

The methodology presented in this section consists of measuring the total transferred charge at two different particular pH values while one of the phases is stirred at the same convection velocity. Later on, the total transferred charge at a given pH vs. the total charge measured at the other selected pH is plotted. In Fig. 1c the total charge at pH 5 (S3) is plotted vs. the total charge at pH 2 (S1) or pH 8 (S2). In general, these two selected pH values, must be an intermediate pH, where both mechanisms coexist in similar proportions, and an extreme pH, where only one mechanism prevails (reaction (I) at low pH or reaction (II) at high pH).

As it was pointed out, the species distribution of the system changes substantially for different pH values, and the total transferred charge changes when FHCs are applied. Consequently, the basis of the method is to establish what kind of proportionality exists between the total charges obtained under different convection regimes.

### 3.2.1. Methodology based on FHCs in organic phase

The methodology involves the construction of working curves of the total charge transferred vs. convection velocities at different pH values. As shown in Fig. 1b, when FHCs are applied to the organic phase, the total charge increases monotonously with increasing convection velocity. Plotting the total charge measured in S3 vs the total charge measured in S2 it is possible to show that the total charges in both experimental conditions are directly proportional to each other. Note that the total charge in quiescent conditions has been subtracted from the total charge ($\Delta Q = q^{v_x^o} - q^{v_x^o=0}$). This behaviour is due to changes in the distribution of species in the system, and, in particular, the concentration changes in the organic phase where the perturbation is applied to mass transport. The distribution of species in partition and acid-base equilibria can be found from the equations recently developed by Garcia et al. [25]. In particular, neutral weak base concentration in the organic phase, $c_B^o$, can be calculated according to the following expression:

$$c_B^o = c_B^{init}\left[\frac{\alpha_B K_{D,B}}{1 + r\alpha_B K_{D,B}}\right] \quad (4)$$

where $\alpha_B = \frac{K_{a,HB^+}^w}{c_{H^+}^w + K_{a,HB^+}^w}$ and $c_B^{init}$ is the initial concentration of the weak base. Clearly, the neutral weak base concentration in the organic phase is defined by the pH value and the volume ratio of aqueous and organic phases. FHCs applied to the organic phase produce changes in the total charge with respect to the system under quiescent conditions, which are directly proportional to the concentration of neutral weak base in the organic phase. Hence, the proportionality constant (slope) can be written as:

$$a = \frac{\Delta Q_{\mathrm{pHS3}}}{\Delta Q_{\mathrm{pHS2}}} = \frac{q_{\mathrm{pHS3}}^{v_x^o} - q_{\mathrm{pHS3}}^{v_x^o=0}}{q_{\mathrm{pHS2}}^{v_x^o} - q_{\mathrm{pHS2}}^{v_x^o=0}} = \frac{c_{\mathrm{B}}^{\mathrm{init}} \left( \frac{\alpha_{\mathrm{B,S3}} K_{\mathrm{D,B}}}{1 + r\alpha_{\mathrm{B,S3}} K_{\mathrm{D,B}}} \right) g(v, v_x^o, D_{\mathrm{species}}^{\alpha})}{c_{\mathrm{B}}^{\mathrm{init}} \left( \frac{\alpha_{\mathrm{B,S2}} K_{\mathrm{D,B}}}{1 + r\alpha_{\mathrm{B,S2}} K_{\mathrm{D,B}}} \right) g(v, v_x^o, D_{\mathrm{species}}^{\alpha})} \tag{5}$$

Where $q_{\mathrm{pH}}^{v_x^o=0}$ and $q_{\mathrm{pH}}^{v_x^o}$ are the total charge obtained without and with FHCs applied to the organic phase, respectively, and $g(v, v_x^o, D_{\mathrm{species}}^{\alpha})$ is a function which is derived from the integration of the current obtained by applying FHCs. $g(v, v_x^o, D_{\mathrm{species}}^{\alpha})$ depends on the sweep rate, the convection velocity, the diffusion coefficients of the species and the hydrodynamic properties of the solvents. Considering that the effects of the neutral weak base concentration do not affect the hydrodynamic properties of the solvents, the $g(v, v_x^o, D_{\mathrm{species}}^{\alpha})$ value can be considered constant at different pH values without loss of generality of the methodology. Hence, the slope can be rewritten as:

$$a = \frac{\alpha_{\mathrm{B,S3}}}{\alpha_{\mathrm{B,S2}}} \left[ \frac{1 + r\alpha_{\mathrm{B,S2}} K_{\mathrm{D,B}}}{1 + r\alpha_{\mathrm{B,S3}} K_{\mathrm{D,B}}} \right] \tag{6}$$

and from this expression it is possible to know the value of the partition constant of the neutral weak base.

At both the negative and positive extremes of $\log(r)$, the proportionality constant (Eq. (6)) reaches limiting values. The limiting behaviour of *a* is shown in Fig. 2 and can be represented as follows:

$$\lim_{r \to 0} a = \frac{\alpha_{\mathrm{B,S3}}}{\alpha_{\mathrm{B,S2}}} = a_{r \to 0} \tag{7}$$

and,

$$\lim_{r \to \infty} a = 1 \tag{8}$$

therefore, the possible values of the slope are bounded to $a_{r \to 0} \le a \le 1$.

According to Eq. (7), the proportionality constant (Eq. (6)) can be normalized as:

$$\frac{a}{a_{r\to 0}} = \left[\frac{1+r\alpha_{\mathrm{B,S2}}K_{\mathrm{D,B}}}{1+r\alpha_{\mathrm{B,S3}}K_{\mathrm{D,B}}}\right] \tag{9}$$

and the $K_{\mathrm{D,B}}$ value can be obtained from the following equation:

$$K_{\mathrm{D,B}} = \frac{1-\left(\frac{a}{a_{r\to 0}}\right)}{r\left[\left(\frac{a}{a_{r\to 0}}\right)\alpha_{\mathrm{B,S3}} - \alpha_{\mathrm{B,S2}}\right]} \tag{10}$$

Finally, we analyze the analytical validity of the procedure proposed. According to Eq. (9), in order to calculate $K_{\mathrm{D,B}}$ it is necessary to analyse the behaviour of the term $1+r\alpha_{\mathrm{B}}K_{\mathrm{D,B}}$ as a function of $\log(r)$ at both pH values (S2 and S3). Fig. 3 shows that when $r\to 0$, the $1+r\alpha_{\mathrm{B}}K_{\mathrm{D,B}}$ values are close to unit for both pH values. In this experimental condition, it is not possible to obtain the partition coefficient value. On the other hand, if $r>>1$ then $r\alpha_{\mathrm{B}}K_{\mathrm{D,B}}>>1$ for both conditions, so $a=1$ (Eq. (6)) and the partition coefficient value is inaccessible by the methodology proposed in this work. If proper experimental conditions are chosen it is possible to determine the partition coefficient. Optimal conditions can be obtained from an estimated value of $K_{\mathrm{D,B}}$, the value of acid dissociation constant, pH and volume ratio (see Fig. 3). As an example, for $-2.5<\log(r)<0.0$, an error of less than 5.0% in the value of the partition coefficient is obtained. An optimal experimental condition is to use a volume ratio range that ensures that $1+r\alpha_{\mathrm{B,S2}}K_{\mathrm{D,B}}$ is high enough and $1+r\alpha_{\mathrm{B,S3}}K_{\mathrm{D,B}}$ is close to one. In this way, the simplified expression for $K_{\mathrm{D,B}}$ can be expressed as follows:

$$K_{\mathrm{D,B}} = \frac{\left(\frac{a}{a_{r\to 0}}\right) - 1}{r\alpha_{\mathrm{B,S2}}} \tag{11}$$

To examine the optimal conditions for determining the partition coefficient, Fig. 4 shows the $K_{\mathrm{D,B}}$ values obtained for different volume ratios. As described above, when $a$ results independent of $K_{\mathrm{D,B}}$ (for $r >> 1$) the partition coefficient values are unpredictable, and if $a = a_{r\to 0}$ the results are higher than the exact values. For that reason, the correct procedure to determine $K_{\mathrm{D,B}}$ for this methodology, given the following conditions, would be:

$$a_{r\to 0} < a < 1 \tag{12}$$

and

$$-2.5 < \log(r) < 0 \tag{13}$$

### 3.2.2. Methodology based on FHCs in aqueous phase

The same procedure presented in the previous Section can be extended to the case when FHCs are applied to the aqueous phase. The experimental conditions of the systems S1 and S3 (Fig. 1a) must be considered, and the concentration of $HB^+$ and B species present in the aqueous phase defining the proportionality constant (Fig. 1c). The total concentration of species in the aqueous phase, $c^{\mathrm{w}}_{\mathrm{Btot}}\left(= c^{\mathrm{w}}_{\mathrm{B}} + c^{\mathrm{w}}_{\mathrm{HB^+}}\right)$, is defined by [25]:

$$c^{\mathrm{w}}_{\mathrm{Btot}} = c^{\mathrm{init}}_{\mathrm{B}} \left[\frac{1}{1 + r\alpha_{\mathrm{B}} K_{\mathrm{D,B}}}\right] \tag{14}$$

and the proportionality constant by:

$$a = \frac{1 + r\alpha_{\mathrm{B,S1}} K_{\mathrm{D,B}}}{1 + r\alpha_{\mathrm{B,S3}} K_{\mathrm{D,B}}} \tag{15}$$

Finally, the $K_{\mathrm{D,B}}$ value can be obtained according to the following equation:

$$K_{\mathrm{D,B}} = \frac{a - 1}{r\left(\alpha_{\mathrm{B,S1}} - a\alpha_{\mathrm{B,S3}}\right)} \tag{16}$$

### 3.3. Description of the methodology based on FHCs at constant pH

Another simple way to determine the partition coefficient for protonatable neutral base is a methodology based on measurement of the total charge transferred as a function of an external parameter such as volume ratio. As in Section 3.2.1, the analysis is focused on the application of FHCs to the organic phase.

Considering a constant volume ratio, the difference between the charges ($\Delta Q$) obtained with quiescent solutions ($q_{\mathrm{r}}^{v_x^{\mathrm{o}}=0}$) and applying FHCs ($q_{\mathrm{r}}^{v_x^{\mathrm{o}}}$) can be expressed as follows:

$$\Delta Q = q_{\mathrm{r}}^{v_x^{\mathrm{o}}} - q_{\mathrm{r}}^{v_x^{\mathrm{o}}=0} = c_{\mathrm{B}}^{\mathrm{init}} \left( \frac{\alpha_{\mathrm{B}} K_{\mathrm{D,B}}}{1 + r\alpha_{\mathrm{B}} K_{\mathrm{D,B}}} \right) g(v, v_x^{\mathrm{o}}, D_{\mathrm{species}}^{\alpha}) \tag{17}$$

Taking the reciprocal of both sides in Eq. (17), the following equation is obtained:

$$(\Delta Q)^{-1} = \left( \frac{1}{\alpha_{\mathrm{B}} K_{\mathrm{D,B}}} \right) \left( \frac{1}{c_{\mathrm{B}}^{\mathrm{init}} g(v, v_x^{\mathrm{o}}, D_{\mathrm{species}}^{\alpha})} \right) + r \left( \frac{1}{c_{\mathrm{B}}^{\mathrm{init}} g(v, v_x^{\mathrm{o}}, D_{\mathrm{species}}^{\alpha})} \right) \tag{18}$$

A plot of $(\Delta Q)^{-1}$ versus $r$ yields a straight line with an ordinate intercept of $\left[ c_{\mathrm{B}}^{\mathrm{init}} \alpha_{\mathrm{B}} K_{\mathrm{D,B}} g(v, v_x^{\mathrm{o}}, D_{\mathrm{species}}^{\alpha}) \right]^{-1}$ and a slope of $\left[ c_{\mathrm{B}}^{\mathrm{init}} g(v, v_x^{\mathrm{o}}, D_{\mathrm{species}}^{\alpha}) \right]^{-1}$. The intercept on the horizontal axis is $-\left[ \alpha_{\mathrm{B}} K_{\mathrm{D,B}} \right]^{-1}$. Importantly, this volume ratio ($r < 0$) has no real physical meaning, but can be mathematically extrapolated to easily calculate the partition coefficient value.

By measuring $\Delta Q$ for different volume ratios $K_{\mathrm{D,B}}$ can be obtained from ordinate intercept and slope values (linear regression analysis according to Eq. (18)):

$$K_{\mathrm{D,B}} = \left( \frac{K_{\mathrm{a}}^{\mathrm{w}} + c_{\mathrm{H^+}}^{\mathrm{w}}}{K_{\mathrm{a}}^{\mathrm{w}}} \right) \left( \frac{\text{slope value}}{\text{intercept value}} \right) \tag{19}$$

### 3.4. Description of the methodology based on FHCs varying pH

A fourth way to determine the $K_{\mathrm{D,B}}$ value is a methodology based on the measurement of the total charge transferred as a function of an external parameter such as pH. As in Section 3.2.1, the analysis is focused on the application of FHCs to the organic phase.

Considering a constant pH, the difference between the charges ($\Delta Q$) obtained with quiescent solutions ($q_{\mathrm{pH}}^{v_x^{\mathrm{o}}=0}$) and applying FHCs ($q_{\mathrm{pH}}^{v_x^{\mathrm{o}}}$) can be expressed as follows:

$$\Delta Q = q_{\mathrm{pH}}^{v_x^{\mathrm{o}}} - q_{\mathrm{pH}}^{v_x^{\mathrm{o}}=0} = c_{\mathrm{B}}^{\mathrm{init}} \left( \frac{\alpha_{\mathrm{B}} K_{\mathrm{D,B}}}{1 + r\alpha_{\mathrm{B}} K_{\mathrm{D,B}}} \right) g(v, v_x^{\mathrm{o}}, D_{\mathrm{species}}^{\alpha}) \tag{20}$$

Taking the reciprocal of both sides in Eq. (20), the following equation is obtained:

$$(\Delta Q)^{-1} = \frac{1}{\alpha_{\mathrm{B}}} \left( \frac{1}{K_{\mathrm{D,B}} c_{\mathrm{B}}^{\mathrm{init}} g(v, v_x^{\mathrm{o}}, D_{\mathrm{species}}^{\alpha})} \right) + \left( \frac{r}{c_{\mathrm{B}}^{\mathrm{init}} g(v, v_x^{\mathrm{o}}, D_{\mathrm{species}}^{\alpha})} \right) \tag{21}$$

A plot of $(\Delta Q)^{-1}$ versus $\alpha_{\mathrm{B}}{}^{-1}$ yields a straight line with an ordinate intercept of $r\left[ c_{\mathrm{B}}^{\mathrm{init}} g(v, v_x^{\mathrm{o}}, D_{\mathrm{species}}^{\alpha}) \right]^{-1}$ and a slope of $\left[ K_{\mathrm{D,B}} c_{\mathrm{B}}^{\mathrm{init}} g(v, v_x^{\mathrm{o}}, D_{\mathrm{species}}^{\alpha}) \right]^{-1}$. The intercept on the horizontal axis is $-rK_{\mathrm{D,B}}$. In the same way as in the previous section, this $\alpha_{\mathrm{B}}$ ($\alpha_{\mathrm{B}} < 0$) has no real physical meaning, but can be mathematically extrapolated to easily calculate the partition coefficient value.

By measuring $\Delta Q$ for different pH values, $K_{D,B}$ can be obtained from ordinate intercept and slope values (linear regression analysis according to Eq. (21)):

$$K_{D,B} = r^{-1}\left(\frac{\text{intercept value}}{\text{slope value}}\right) \tag{22}$$

### 3.5. Validation of the electrochemical approach from simulated results by finite element method and velocity field measurements

In this section, FEM results are first compared to experimental velocity field measurements and then used to validate the proposed methodology. The focus is directed to obtain the fluid velocity field, and then couple the electrochemical reactions that represent the transfer of protonated species. In addition, these results will be used to validate the approach of the proposed one-dimensional model. COMSOL Multiphysics finite element package [81] (COMSOL version 4.2a) was used to calculate the fluid velocity field, $\mathbf{u}$, by solving the continuity and Navier–Stokes equations for an incompressible, isothermal flow at low Mach number. In this computational fluid dynamics (CFD) model the flow is laminar. To determine the charge flux and provide additional insight into the ion transfer process, the electrochemical reactions were in some cases taken into account along the CFD model. Simple CFD simulations were carried out in a full 3D model in order to compare with MRI measurements, while coupled electrochemical and CFD simulations were carried out in a 2D model representing a 3D system with cylindrical symmetry. For experimental simplicity, the upper phase in the former case was an aqueous solution, while for the latter, 1,2-dichloroethane was used. The geometry of the cell matched the experimental cell

geometry in all cases (see Fig. 5). No-slip boundary conditions are imposed at the boundaries corresponding to the cell walls and bottom. Rotational boundary conditions are considered at the bottom of the rod ( $z = h_1 - h_3, r < r_3,\ \mathbf{u} = \omega \times \mathbf{r}$, where $\omega$ is the angular velocity of cylinder rotation) and at the shaft of the cylinder ( $h_1 > z > h_1 - h_3, r = r_3, \mathbf{u} = \omega \times \mathbf{r_3}$ ). The mesh used in cylindrical coordinates was automatically generated by the software. Grid and time step independence of the results was checked. Additionally, since the experimental measurements showed that the organic solvent below the glass plate was not affected by the convection of the upper phase (data not shown), only the latter was incorporated into the 2D and 3D simulations and no-slip boundary conditions were employed at the interfacial zone. Firstly, we turn our attention to the flow pattern generated inside electrochemical cell.

A comparison between the simulated and experimental *z*-velocity maps corresponding to $\omega = 62.8\,\mathrm{s}^{-1}\,(600\,\mathrm{rpm})$ rotational speed of the upper phase is presented in Fig. 6. Experimental maps, on the right, are limited within the NMR sensitive volume. The hydrodynamic behavior from FEM and velocity imaging show an extraordinary correspondence, even if the velocity scale slightly differs. This validates the assumption that the flow regime inside the cell is laminar. A circulation of fluid below and on the side of the rotating cylinder can be clearly observed; the liquid moves towards the bottom of the cell through the outer region, close to the wall of the cell, and returns to the cylinder through the central section[65]. This flow represents the main mass transfer process that takes place in the system.

MRI showed that the rotating rod was not perfectly aligned with the glass cell. Thus, the 3D model for the FEM simulation was constructed with an offset of 0.7 mm

between their axes. Fig. 6a and 6b correspond to plane *xz* and Fig. 6c and 6d corresponds to *yz*, where the offset is observed. This suggests that the main source of asymmetry in the velocity map below the rod is due to this offset. In the Supplementary Material (Section A3), the CFD calculation for the symmetrical cell configuration is presented, where identical velocity maps both planes are obtained. The horizontal cuts in Fig. 6e to 6h ($Z_1$), show that forced hydrodynamic conditions contribute to move the liquid (and eventually dissolved species) towards and from the interface. The cuts nearest to the interfacial zone in Fig. 6g and 6h ($Z_2$) are of special interest since this region is the source of the electrochemical signal.

In order to perform a quantitative analysis of normal velocities near the liquid|liquid interface, , which takes into account the electrochemical processes, *z*-velocity profiles obtained from the 2D axisymmetric model are shown for different *z*-axis values near the interface (see Fig. 7). The general behaviour observed is that for large radius values, the fluid moves towards the interface, whereas towards the middle of the cell, the fluid tends to move away from it. The area where the fluid moves towards the interface yields the highest contribution to the total ion transfer current. This is the main reason why the one-dimensional model (Section 1.2), for which convection carries the species toward the interface, provides qualitatively comparable electrochemical signals with the CFD model.

The validation of the methodology was carried out using the 2D model with coupled electrochemistry and forced hydrodynamic conditions. Several simulations were carried out for different pH and rotation speed values. In order to determine $K_{D,B}$, a linear fit of the total charge measured at pH 4.5 (S3) as a function of the total charge measured at pH 6.8 (S2) was made. The simulation parameters were chosen to represent the Tylosin A, which

is the compound to be used in the next section to experimentally validate the proposed methodology. FHCs were applied to the organic phase. In Fig. 8, $\Delta Q_{\mathrm{pH\,4.5}}$ vs. $\Delta Q_{\mathrm{pH\,6.8}}$ is shown. The slope of this curve is equal to $a = \frac{\alpha_{\mathrm{B,pH\,4.5}}}{\alpha_{\mathrm{B,pH\,6.8}}}\left[\frac{1+r\alpha_{\mathrm{B,pH\,6.8}}K_{\mathrm{D,B}}}{1+r\alpha_{\mathrm{B,pH\,4.5}}K_{\mathrm{D,B}}}\right]$ thus, the partition coefficient can be calculated with this last equation. Considering $\mathrm{p}K^{\mathrm{w}}_{a,\mathrm{HB}^+} = 7.73$ [82] and that the slope value obtained from linear fit of the data plotted in Fig. 8 is $a = (0.251 \pm 0.001)$, the partition coefficient obtained according to Eq. (10) is $\log(K_{\mathrm{D,B}}) = 3.1 \pm 0.2$.

### 3.6. Validation of the electrochemical approach from experimental results

We applied the methodology developed in Section 3.2., for the determination of the partition coefficient between $H_2O$ and 1,2-dichloroethane of the neutral weak base Tylosin A. The current-potential profiles obtained at different rotation speeds applied to the organic phase at two different pH values are shown in Fig. 9 (insets (a) and (b)). In this case, pH values correspond to S2 and S3 systems in Fig 1b. From the integration of the current in the forward potential sweep we can obtain the total charge transferred. In order to determine $K_{\mathrm{D,TylA}}$ a linear fit of the total charge measured at pH 4.5 (S3) as a function of the total charge measured at pH 6.8 (S2) was made. A constant volume ratio value ($r = 0.48$) was employed. In Fig. 9, $\Delta Q_{\mathrm{pH\,4.5}}$ as a function of $\Delta Q_{\mathrm{pH\,6.8}}$ is shown. The slope of this curve is equal to $a = \frac{\alpha_{\mathrm{TylA,pH\,4.5}}}{\alpha_{\mathrm{TylA,pH\,6.8}}}\left[\frac{1+r\alpha_{\mathrm{TylA,pH\,6.8}}K_{\mathrm{D,TylA}}}{1+r\alpha_{\mathrm{TylA,pH\,4.5}}K_{\mathrm{D,TylA}}}\right]$ thus, the partition coefficient can be calculated with this last equation. Considering $\mathrm{p}K^{\mathrm{w}}_{a,\mathrm{HTylA}^+} = 7.73$ [82] and that the slope

value obtained from linear fit of the data plotted in Fig. 8 is $a = (0.34 \pm 0.02)$, the partition coefficient obtained according to Eq. (10) is $\log(K_{D,TylA}) = 3.3 \pm 0.2$. It is important to highlight that the slope value obtained is in agreement with the optimal experimental criteria (volume ratio and pH) for determining the partition coefficient of neutral weak bases discussed above (see Fig. 2). The calculation of the uncertainty associated with this partition coefficient value is developed in the Appendix. The partition coefficient value obtained in this work is in good agreement with a previous result reported in literature [27].

**Conclusion**

An original electrochemical methodology for the determination of the partition coefficient of neutral weak bases was introduced. The application of mechanical stirring to one of the phases during the potential sweep was used as an effective tool to obtain this thermodynamic parameter. The general equations for a model that describes facilitated proton transfer reactions across the oil|water interface assisted by a weak base under forced hydrodynamic conditions were developed and the entire method has been validated by experimental results and computer simulations of increasing complexity. A great advantage of the methodology presented here is the possibility of measuring the total charge transferred as a function of the convection velocities. The fundamental equations that allow obtaining the partition coefficient of a neutral weak base using only two measurements at different pH were developed in this work. Furthermore, we defined the criteria (volume ratio and pH) for determining the partition coefficient of neutral weak bases in optimal experimental conditions. In addition, several practical equations established to calculate

partition coefficient using pH or volume ratio as variables. Finally, the velocity fields obtained by FEM calculations were successfully corroborated by MRI measurements.

**Acknowledgements**

M.I.V., R.A.F., R.H.A. and S.A.D. are Researchers from Consejo Nacional de Investigaciones Científicas y Tecnológicas (CONICET). F.M.Z., J.M.O., F.V.M. and M.R.S. thank CONICET for the fellowships granted. Financial support from CONICET, Secretaría de Ciencia y Tecnología de la Universidad Nacional de Córdoba (SECyT-UNC) and Fondo para la Investigación Científica y Tecnológica (FONCyT) PICT-2012-1820 are gratefully acknowledged.

**Appendix**

In this appendix, the equations to obtain the uncertainty associated with the partition coefficient ($\sigma_{K_{D,\mathrm{B}}}$) are developed. $\sigma_{K_{D,\mathrm{B}}}$ is defined by the measurable parameters in the system, i.e. $r$, $\mathrm{pH}_{\mathrm{S2}}$, $\mathrm{pH}_{\mathrm{S3}}$, $\mathrm{p}K^{\mathrm{w}}_{a,\mathrm{HB}^+}$ and $a$. For simplicity, we consider a constant temperature.

Special care must be taken regarding some key factors: distance from the rod to the liquid|liquid interface, volume of solution added to the cell (especially the upper phase) and alignment between the center of the glass cell and the rod's axis. Once the experimental procedure has been optimized in order for these factors to be reproducible, the uncertainty can be calculated following the equations developed in this appendix.

Eq. (10) in the body of the work can be rewritten as:

$$K_{D,\mathrm{B}} = \frac{1}{r}\left[\frac{a\times 10^{\mathrm{p}K^{\mathrm{w}}_{a,\mathrm{HB}^+}-\mathrm{pH}_{\mathrm{S3}}} - 10^{\mathrm{p}K^{\mathrm{w}}_{a,\mathrm{HB}^+}-\mathrm{pH}_{\mathrm{S2}}}}{(1-a)} - 1\right] \tag{B1}$$

the absolute uncertainty in $K_{\mathrm{D,B}}$ is calculated as follow:

$$\begin{aligned}\left(\sigma_{K_{D,\mathrm{B}}}\right)^2 = &\left(\frac{\partial K_{D,\mathrm{B}}}{\partial r}\sigma_r\right)^2 + \left(\frac{\partial K_{D,\mathrm{B}}}{\partial a}\sigma_a\right)^2 + \left(\frac{\partial K_{D,\mathrm{B}}}{\partial \mathrm{pH}_{\mathrm{S3}}}\sigma_{\mathrm{pH}_{\mathrm{S3}}}\right)^2 \\ &+ \left(\frac{\partial K_{D,\mathrm{B}}}{\partial \mathrm{pH}_{\mathrm{S2}}}\sigma_{\mathrm{pH}_{\mathrm{S2}}}\right)^2 + \left(\frac{\partial K_{D,\mathrm{B}}}{\partial \mathrm{p}K^{\mathrm{w}}_{a,\mathrm{HB}^+}}\sigma_{\mathrm{p}K^{\mathrm{w}}_{a,\mathrm{HB}^+}}\right)^2\end{aligned} \tag{B2}$$

where $\left(\sigma_r\right)^2 = \left(\frac{\partial r}{\partial V_{\mathrm{w}}}\sigma_{V_{\mathrm{w}}}\right)^2 + \left(\frac{\partial r}{\partial V_{\mathrm{o}}}\sigma_{V_{\mathrm{o}}}\right)^2 = \left(-\frac{V_{\mathrm{o}}}{V_{\mathrm{w}}^2}\sigma_{V_{\mathrm{w}}}\right)^2 + \left(\frac{1}{V_{\mathrm{w}}}\sigma_{V_{\mathrm{o}}}\right)^2$,

$$\frac{\partial K_{D,\mathrm{B}}}{\partial r}\sigma_r = -\frac{K_{D,\mathrm{B}}}{r}\sigma_r, \tag{B3}$$

$$\frac{\partial K_{D,\mathrm{B}}}{\partial a}\sigma_a = \frac{1}{r(1-a)^2}\left(10^{\mathrm{p}K^{\mathrm{w}}_{a,\mathrm{HB}^+}-\mathrm{pH}_{\mathrm{S3}}} - 10^{\mathrm{p}K^{\mathrm{w}}_{a,\mathrm{HB}^+}-\mathrm{pH}_{\mathrm{S2}}}\right)\sigma_a, \tag{B4}$$

$$\frac{\partial K_{D,\mathrm{B}}}{\partial \mathrm{pH}_{\mathrm{S3}}}\sigma_{\mathrm{pH}_{\mathrm{S3}}} = -\frac{a\times\ln(10)}{r(1-a)}\left(10^{\mathrm{p}K^{\mathrm{w}}_{a,\mathrm{HB}^+}-\mathrm{pH}_{\mathrm{S3}}}\right)\sigma_{\mathrm{pH}_{\mathrm{S3}}}, \tag{B5}$$

$$\frac{\partial K_{D,\mathrm{B}}}{\partial \mathrm{pH}_{\mathrm{S2}}}\sigma_{\mathrm{pH}_{\mathrm{S2}}} = \frac{\ln(10)}{r(1-a)}\left(10^{\mathrm{p}K^{\mathrm{w}}_{a,\mathrm{HB}^+}-\mathrm{pH}_{\mathrm{S2}}}\right)\sigma_{\mathrm{pH}_{\mathrm{S2}}} \tag{B6}$$

and

$$\frac{\partial K_{D,\mathrm{B}}}{\partial \mathrm{p}K^{\mathrm{w}}_{a,\mathrm{HB}^+}}\sigma_{\mathrm{p}K^{\mathrm{w}}_{a,\mathrm{HB}^+}} = \frac{\ln(10)}{r(1-a)}\left(a\times 10^{\mathrm{p}K^{\mathrm{w}}_{a,\mathrm{HB}^+}-\mathrm{pH}_{\mathrm{S3}}} - 10^{\mathrm{p}K^{\mathrm{w}}_{a,\mathrm{HB}^+}-\mathrm{pH}_{\mathrm{S2}}}\right)\sigma_{\mathrm{p}K^{\mathrm{w}}_{a,\mathrm{HB}^+}} \tag{B7}$$

Finally, replacing Eqs. (B3)-(B7) in Eq. (B2) we obtained the uncertainty associated to partition coefficient:

$$\left(\sigma_{K_{D,\mathrm{B}}}\right)^2 = \left(-\frac{K_{D,\mathrm{B}}}{r}\right)^2 \left[\left(-\frac{V_\mathrm{o}}{V_\mathrm{w}^2}\sigma_{V_\mathrm{w}}\right)^2 + \left(\frac{1}{V_\mathrm{w}}\sigma_{V_\mathrm{o}}\right)^2\right] + \left[\frac{1}{r(1-a)^2}\left(10^{\mathrm{p}K^{\mathrm{w}}_{a,\mathrm{HB}^+}-\mathrm{pH}_{\mathrm{S3}}} - 10^{\mathrm{p}K^{\mathrm{w}}_{a,\mathrm{HB}^+}-\mathrm{pH}_{\mathrm{S2}}}\right)\sigma_a\right]^2 + \left[-\frac{a\times\ln(10)}{r(1-a)}\left(10^{\mathrm{p}K^{\mathrm{w}}_{a,\mathrm{HB}^+}-\mathrm{pH}_{\mathrm{S3}}}\right)\sigma_{\mathrm{pH}_{\mathrm{S3}}}\right]^2 + \left[\frac{\ln(10)}{r(1-a)}\left(10^{\mathrm{p}K^{\mathrm{w}}_{a,\mathrm{HB}^+}-\mathrm{pH}_{\mathrm{S2}}}\right)\sigma_{\mathrm{pH}_{\mathrm{S2}}}\right]^2 + \left[\frac{\ln(10)}{r(1-a)}\left(a\times10^{\mathrm{p}K^{\mathrm{w}}_{a,\mathrm{HB}^+}-\mathrm{pH}_{\mathrm{S3}}} - 10^{\mathrm{p}K^{\mathrm{w}}_{a,\mathrm{HB}^+}-\mathrm{pH}_{\mathrm{S2}}}\right)\sigma_{\mathrm{p}K^{\mathrm{w}}_{a,\mathrm{HB}^+}}\right]^2 \quad \text{(B8)}$$

## References


[1] Z. Yoshida, H. Freiser, J. Electroanal. Chem. 162 (1984) 307–319.

[2] D. Homolka, V. Mareček, Z.Z. Samec, K. Baše, H.H. Wendt, J. Electroanal. Chem. 163 (1984) 159–170.

[3] Y. Liu, E. Wang, J. Chem. Soc. Faraday Trans. I 83 (1987) 2993–2999.

[4] H. Doe, K. Yoshioka, T. Kitagawa, J. Electroanal. Chem. 324 (1992) 69–78.

[5] L.M. Yudi, A.M. Baruzzi, J. Electroanal. Chem. 328 (1992) 153–164.

[6] K. Kontturi, L. Murtomäki, J. Pharm. Sci. 81 (1992) 970–975.

[7] L.M. Yudi, A.M. Baruzzi, V.M. Solis, J. Electroanal. Chem. 360 (1993) 211–219.

[8] S.A. Dassie, L.M. Yudi, A.M. Baruzzi, Electrochim. Acta 40 (1995) 2953–2959.

[9] F. Reymond, G. Steyaert, A. Pagliara, P. Carrupt, B. Testa, H.H. Girault, Helv. Chim. Acta 79 (1996) 1651–1669.

[10] F. Reymond, G. Steyaert, P.-A. Carrupt, B. Testa, H.H. Girault, J. Am. Chem. Soc. 118 (1996) 11951–11957.

[11] F. Reymond, G. Steyaert, P.-A. Carrupt, B. Testa, H.H. Girault, Helv. Chim. Acta 79 (1996) 101–117.

[12] F. Reymond, P.-F. Brevet, P.-A. Carrupt, H.H. Girault, J. Electroanal. Chem. 424 (1997) 121–139.

[13] Z. Ding, F. Reymond, P. Baumgartner, D.J. Fermín, P.-F. Brevet, P. Carrupt, H.H. Girault, Electrochim. Acta 44 (1998) 3–13.

[14] Y. Kubota, H. Katano, K. Maeda, M. Senda, Electrochim. Acta 44 (1998) 109–116.

[15] Z. Samec, J. Langmaier, A. Trojánek, E. Samcová, J. Málek, Anal. Sci. 14 (1998) 35–41.

[16] S. Sawada, T. Osakai, Phys. Chem. Chem. Phys. 1 (1999) 4819–4825.

[17] F. Reymond, P.-A. Carrupt, B. Testa, H.H. Girault, Chem. Eur. J. 5 (1999) 39–47.

[18] A.I. Azcurra, L.M. Yudi, A.M. Baruzzi, J. Electroanal. Chem. 461 (1999) 194–200.

[19] F. Reymond, V. Chopineaux-Courtois, G. Steyaert, G. Bouchard, P.-A. Carrupt, B. Testa, H.H. Girault, J. Electroanal. Chem. 462 (1999) 235–250.

[20] W. Wickler, A. Mönner, E. Uhlemann, S. Wilke, H. Müller, J. Electroanal. Chem. 469 (1999) 91–96.

[21] M. Senda, Y. Kubota, H. Katano, in:, Liq. Interfaces Chem. Biol. Pharm. Appl., 2001, pp. 683–698.

[22] Y. Kubota, H. Katano, M. Senda, Anal. Sci. 17 (2001) 65–70.

[23] R.A. Fernández, S.A. Dassie, J. Electroanal. Chem. 585 (2005) 240–249.

[24] J.I. Garcia, R.A. Iglesias, S.A. Dassie, J. Electroanal. Chem. 586 (2006) 225–236.

[25] J.I. Garcia, R.A. Fernández, A.J. Ruggeri, S.A. Dassie, J. Electroanal. Chem. 594 (2006) 80–88.

[26] M. Rimboud, C. Elleouet, F. Quentel, J.-M. Kerbaol, M. L'Her, J. Electroanal. Chem. 622 (2008) 233–237.

[27] R.A. Fernández, M.I. Velasco, L.I. Rossi, S.A. Dassie, J. Electroanal. Chem. 650 (2010) 47–54.

[28] J.I. Garcia, M.B. Oviedo, S.A. Dassie, J. Electroanal. Chem. 645 (2010) 1–9.

[29] M. Velický, K.Y. Tam, R.A.W. Dryfe, J. Electroanal. Chem. 683 (2012) 94–102.

[30] M. Velický, K.Y. Tam, R.A.W. Dryfe, Anal. Chem. 84 (2012) 2541–2547.

[31] S.A. Dassie, J. Electroanal. Chem. 728 (2014) 51–59.

[32] F. Vega Mercado, F.M. Zanotto, R.A. Fernández, S.A. Dassie, J. Electroanal. Chem. 774 (2016) 111–121.

[33] F. Vega Mercado, J.M. Ovejero, R.A. Fernández, S.A. Dassie, J. Electroanal. Chem. 765C (2016) 100–104.

[34] S.A. Dassie, J. Electroanal. Chem. 578 (2005) 159–170.

[35] S.A. Dassie, J. Electroanal. Chem. 585 (2005) 256–268.

[36] Z. Samec, Pure Appl. Chem. 76 (2004) 2147–2180.

[37] R.A. Iglesias, S.A. Dassie, Ion Transfer at Liquid|Liquid Interfaces, Nova Publishers, New York, 2010.

[38] G. Taylor, H.H. Girault, J. Electroanal. Chem. 208 (1986) 179–183.

[39] Y. Ohkouchi, T. Kakutani, T. Osakai, M. Senda, Anal. Sci. 7 (1991) 371–376.

[40] J.A. Campbell, H.H. Girault, J. Electroanal. Chem. 266 (1989) 465–469.

[41] A.A. Stewart, G. Taylor, H.H. Girault, J. McAleer, J. Electroanal. Chem. 296 (1990) 491–515.

[42] A.A. Stewart, Y. Shao, C.M. Pereira, H.H. Girault, J. Electroanal. Chem. 305 (1991)

135–139.

[43] J. Koryta, P. Vanýsek, M. Březina, J. Electroanal. Chem. 67 (1976) 263–266.

[44] S. Kihara, M. Suzuki, K. Maeda, K. Ogura, M. Matsui, J. Electroanal. Chem. 210 (1986) 147–159.

[45] S. Wilke, H. Franzke, H. Müller, Anal. Chim. Acta 268 (1992) 285–292.

[46] S. Wilke, Anal. Chim. Acta 295 (1994) 165–172.

[47] B. Hundhammer, T. Solomon, T. Zerihun., M. Abegaz, A. Bekele, K. Graichen, J. Electroanal. Chem. 371 (1994) 1–11.

[48] V. Mareček, H. Jänchenová, M.P. Colombini, P. Papoff, J. Electroanal. Chem. 217 (1987) 213–219.

[49] P. Liljeroth, C. Johans, K. Kontturi, J.A. Manzanares, J. Electroanal. Chem. 483 (2000) 37–46.

[50] S.S. Hill, R.A.W. Dryfe, E.P.L. Roberts, A.C. Fisher, K. Yunus, Anal. Chem. 75 (2003) 486–493.

[51] W.J. Albery, A.M. Couper, J. Hadgraft, C. Ryan, J. Chem. Soc. Faraday Trans. 70 (1974) 1124–1131.

[52] J. Albery, J.F. Burke, E.B. Leffler, J. Hadgraft, J. Chem. Soc. Faraday Trans. 72 (1976) 1618–1626.

[53] W.J. Albery, R.A. Choudhery, J. Phys. Chem. 92 (1988) 1142–1151.

[54] J.A. Manzanares, R. Lahtinen, B. Quinn, K. Kontturi, D.J. Schiffrin, Electrochim. Acta 44 (1998) 59–71.

[55] B. Kralj, R.A.W. Dryfe, J. Phys. Chem. B 106 (2002) 6732–6739.

[56] K. Fujii, S. Tanibuchi, S. Kihara, Anal. Sci. 21 (2005) 1415–1420.

[57] B. Kralj, R.A.W. Dryfe, J. Electroanal. Chem. 560 (2003) 127–133.

[58] N. Wilke, R.A. Iglesias, S.G. Chesniuk, S.A. Dassie, A.M. Baruzzi, Bull. Chem. Soc. Jpn. 75 (2002) 235–240.

[59] M.A. Fernández, L.M. Yudi, A.M. Baruzzi, Electroanalysis 16 (2004) 491–496.

[60] R.A. Fernández, S.A. Dassie, J. Electroanal. Chem. 624 (2008) 121–128.

[61] J.M. Ovejero, R.A. Fernández, S.A. Dassie, J. Electroanal. Chem. 666 (2012) 42–51.

[62] P.T. Callaghan, Principles of Nuclear Magnetic Resonance Microscopy, Clarendon Press, Oxford, 1991.

[63] M.M. Britton, ChemPhysChem 15 (2014) 1731–1736.

[64] L.F. Gladden, A.J. Sederman, J. Magn. Reson. 229 (2013) 2–11.

[65] M. Carpinella, M.I. Velasco, E.V. Silletta, J.M. Ovejero, S.A. Dassie, R.H. Acosta, J. Electroanal. Chem. 750 (2015) 100–106.

[66] E.K. Jeong, S.A. Altobelli, E. Fukushima, E. Jeong, S.A. Altobelli, E. Fukushima, Phys. Fluids 6 (1994) 2901–2906.

[67] S.L. Codd, S.A. Altobelli, J.D. Seymour, J.R. Brown, E.O. Fridjonsson, in:, S.L.

Codd, J.D. Seymour (Eds.), Magn. Reson. Microsc. Spat. Resolv. NMR Tech. Appl., WILEY-VCH Verlag GmbH & Co, Weinheim, Germany, 2009.

[68] J.M. Bray, A.J. Davenport, K.S. Ryder, M.M. Britton, Angew. Chemie - Int. Ed. 55 (2016) 9394–9397.

[69] L. Murtomäki, K. Kontturi, J. Pharm. Sci. 91 (2002) 900–901.

[70] W.G. Cochran, Math. Proc. Cambridge Philos. Soc. 30 (1934) 365–375.

[71] V.G. Levich, Physicochemical Hydrodynamics, Prentice-Hall, Englewood Cliffs, N.J., 1962.

[72] A. Alexiadis, A. Cornell, M.P. Dudukovic, J. Electroanal. Chem. 669 (2012) 55–66.

[73] A.M. Baruzzi, H. Wendt, J. Electroanal. Chem. 279 (1990) 19–30.

[74] A.M. Baruzzi, J. Ühlken, J. Electroanal. Chem. 282 (1990) 267–273.

[75] P.T. Callaghan, Translational Dynamics and Magnetic Resonance: Principles of Pulsed Gradient Spin Echo NMR, Oxford University Press, Philadelphia, 2011.

[76] K.W. Feindel, in:, C. Hartnig, C. Roth (Eds.), Polym. Electrolyte Membr. Direct Methanol Fuel Cell Technol., Woodhead Publishing Limited, 2012, pp. 262–320.

[77] M.M. Britton, P.M. Bayley, P.C. Howlett, A.J. Davenport, M. Forsyth, J. Phys. Chem. Lett. 4 (2013) 3019–3023.

[78] J.M. Bray, A.J. Davenport, K.S. Ryder, M.M. Britton, Angew. Chemie Int. Ed. (2016) 1–5.

[79] A.J. Ilott, N.M. Trease, C.P. Grey, A. Jerschow, Nat. Commun. 5 (2014) 4536–4542.

[80] K. Kose, J. Magn. Reson. 92 (1991) 631–635.

[81] P.W. Pryor, MultiPhysics Modeling Using COMSOL: A First Principles Approach, Jones and Bartlett Publishers, 2011.

[82] J.W. McFarland, C.M. Berger, S.A. Froshauer, S.F. Hayashi, S.J. Hecker, B.H. Jaynes, M.R. Jefson, B.J. Kamicker, C.A. Lipinski, K.M. Lundy, C.P. Reese, C.B. Vu, J. Med. Chem. 40 (1997) 1340–1346.

[83] A. Sabela, V. Mareček, Z. Samec, R. Fuoco, Electrochim. Acta 37 (1992) 231–235.

[84] A.J. Olaya, M. a. Méndez, F. Cortes-Salazar, H.H. Girault, J. Electroanal. Chem. 644 (2010) 60–66.

[85] P. Vanýsek, in:, D.R. Lide (Ed.), Handb. Chem. Phys., 85th Ed., C.R.C. Press New York, 2005, p. 93–95 (Section 5).

**Figure Captions**

**Figure 1: (a)** Charge transferred as function of pH for quiescent solutions (●) and for FHCs applied to aqueous phase (▲) or organic phase (▼). $v_x^{\alpha} = 3.0\times10^{-3}\,\mathrm{cm\,s^{-1}}$. Three different pH values chosen as reference: S1 to pH 2.0; S2 to pH 8.0; and S3 to pH 5.0. **(b)** Effect of $v_x^{\alpha}$ on charge transferred at different pH values: FHCs applied to aqueous phase (●) pH 2.0 and (●) pH 5.0; and FHCs applied to organic phase (▼) pH 5.0 and (▲) pH 8.0. **(c)** Charge obtained for the system S3 as a function of the charge obtained with S2 (organic phase stirred, (○)) or charge obtained with S1 (aqueous phase stirred, (●)).

Simulation parameters: $c_B^{\mathrm{init}} = 1.00\times10^{-3}\,\mathrm{M}$; $\Delta_o^w\phi^{o'}_{HB^+} = -0.023\,\mathrm{V}$; $\Delta_o^w\phi^{o'}_{H^+} = 0.550\,\mathrm{V}$ [83]; $\Delta_o^w\phi^{o'}_{OH^-} = -0.700\,\mathrm{V}$ [84]; $D^w_{H^+} = 9.31\times10^{-5}\,\mathrm{cm^2s^{-1}}$ [85]; $D^o_{H^+} = 1.00\times10^{-5}\,\mathrm{cm^2s^{-1}}$ [83]; $D^w_{OH^-} = 5.27\times10^{-5}\,\mathrm{cm^2s^{-1}}$ [85]; $D^w_{HB^+} = 1.00\times10^{-6}\,\mathrm{cm^2s^{-1}}$; $D^w_B = 1.00\times10^{-6}\,\mathrm{cm^2s^{-1}}$ and $v = 0.015\,\mathrm{Vs^{-1}}$.

**Figure 2:** Dependence of the proportionality constant (slope) values with the logarithm of volume ratio. Simulation parameters are the same as those reported in Fig. 1.

**Figure 3:** Dependence of the factor $1+r\alpha_B K_{D,B}$, from Eq. (9), with the logarithm of volume ratio for two different systems: S2 (·····) and S3 (——). Simulation parameters are the same as those reported in Fig. 1.

**Figure 4:** Ratio between obtained ($K_{D,B}$) from simulation and the true value of partition coefficient, as a function of the logarithm of the volume ratio. Error bars represent an uncertainty associated with the partition coefficient ratio equal to 5.0%. Simulation parameters are the same as those reported in Fig. 1.

Figure 5: Geometry of the cell. Two models are used, 2D models, which are characterized with axisymmetric representation, and 3D models where a representation of the whole cell is performed. All lengths are expressed in mm.

2D model: $h_1$ = 25.1; $h_2$ = 10.0; $h_3$ = 15.0; $h_4$ = 0.1; $h_5$ = 0.1; $r_1$ = 4.5; $r_2$ = 2.4 and $r_3$ = 3.0.

3D model: $h_1$ = 47.7; $h_2$ N/A; $h_3$ = 37.6; $h_4$ = 0.9; $h_5$ N/A; $r_1$ = 7.4; $r_2$ = 2.5 and $r_3$ = 3.0.

**Figure 6:** *z*-velocity maps obtained from CFD for 3D model and from MRI at $\omega = 62.8\,\mathrm{s}^{-1}$. Panels (a), (c), (e) and (g) on the left correspond to simulations and panels (b), (d), (f) and (h) on the right correspond to MRI. Panels (a) and (b) represent the *xz*-cut plane and panels (c) and (d) represent the *yz*-cut plane. Panels (e)-(h) represent *xy*-cut planes at *z*-positions $Z_1$ and $Z_2$, in this order.

Simulation parameters: water: density = $0.9996\,\mathrm{kg\,m}^{-3}$ and dynamic viscosity = $1.009\times10^{-3}\,\mathrm{Pa\,s}$.

**Figure 7:** *z*-velocity profiles obtained from CFD corresponding to $\omega = 62.8\,\mathrm{s}^{-1}$ for 2D axisymmetric model, at different distances in *z*-component to the interface. *z* = 0.02 (——); 0.04 (——); 0.06 (——); 0.08 (——) and 0.10 mm (——). Simulation parameters: 1,2-dichloroethane: density = $1253\,\mathrm{kg\,m}^{-3}$ and dynamic viscosity = $0.8385\times10^{-3}\,\mathrm{Pa\,s}$. Simulation parameters for water are the same as in Fig. 6.

**Figure 8:** Charge obtained from simulations for 2D axisymmetric model for pH 4.5 (S3), as a function of charge obtained for pH 6.8 (S2) when FHCs are applied to organic phase. Rotation speed: (1) 31.4; (2) 41.9; (3) 52.3; (4) 62.8; (5) 73.3; (6) 83.7 and (7) 94.2 $\mathrm{s}^{-1}$.

Simulation parameters: $c_{\mathrm{B}}^{\mathrm{init}} = 1.000\,\mathrm{x}10^{-3}\,\mathrm{M}$; $\mathrm{p}K_{\mathrm{a,\,HB^+}}^{\mathrm{w}} = 7.73$ [82]; $\Delta_{\mathrm{o}}^{\mathrm{w}}\phi_{\mathrm{HB^+}}^{o'} = -0.023\,\mathrm{V}$ [27]; $\log\left(K_{\mathrm{D,B}}\right) = 3.10$ [27]; $D_{\mathrm{HB^+}}^{\mathrm{w}} = 3.4\times10^{-10}\,\mathrm{m^2s^{-1}}$ [27]; $D_{\mathrm{HB^+}}^{\mathrm{o}} = 4.3\times10^{-10}\,\mathrm{m^2s^{-1}}$ [27]; $D_{\mathrm{B}}^{\mathrm{w}} = 3.4\times10^{-10}\,\mathrm{m^2s^{-1}}$ [27]; $D_{\mathrm{B}}^{\mathrm{o}} = 4.7\times10^{-10}\,\mathrm{m^2s^{-1}}$ [27]; $r = 0.4$ and $v = 0.015\,\mathrm{Vs}^{-1}$. Other simulation parameters are the same as those reported in Fig. 7.

**Figure 9:** Tylosin A transfer across water|1,2-dichloroethane interface. Charge obtained for pH values chosen as reference in this case 4.5 (S3), as a function of charge obtained for pH 6.8 (S2). Inset: experimental cyclic voltammograms obtained at two different pH values: pH 4.5 (panel **(a)**), and pH 6.8 (panel **(b)**) obtained for FHCs applied to organic phase. Stirring frequency: (1) 0; (2) 600; (3) 900; and (4) 1200 rpm.

Organic phase: TPADCC $1.0\mathrm{x}10^{-2}$ M. Aqueous phase: KCl $1.0\times10^{-2}$ M + $1.0\times10^{-3}$ M of Tylosin A. r = 0.4; *v* = 0.015 V $\mathrm{s}^{-1}$.

Figure 1a: Vega Mercado et al.

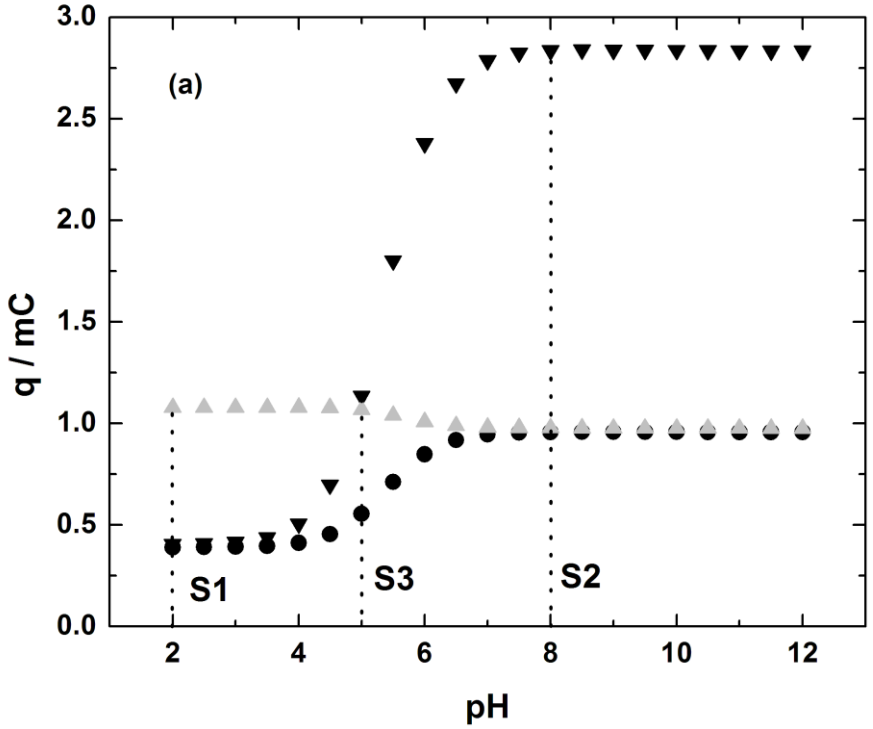


Figure 1a

Figure 1b: Vega Mercado et al.

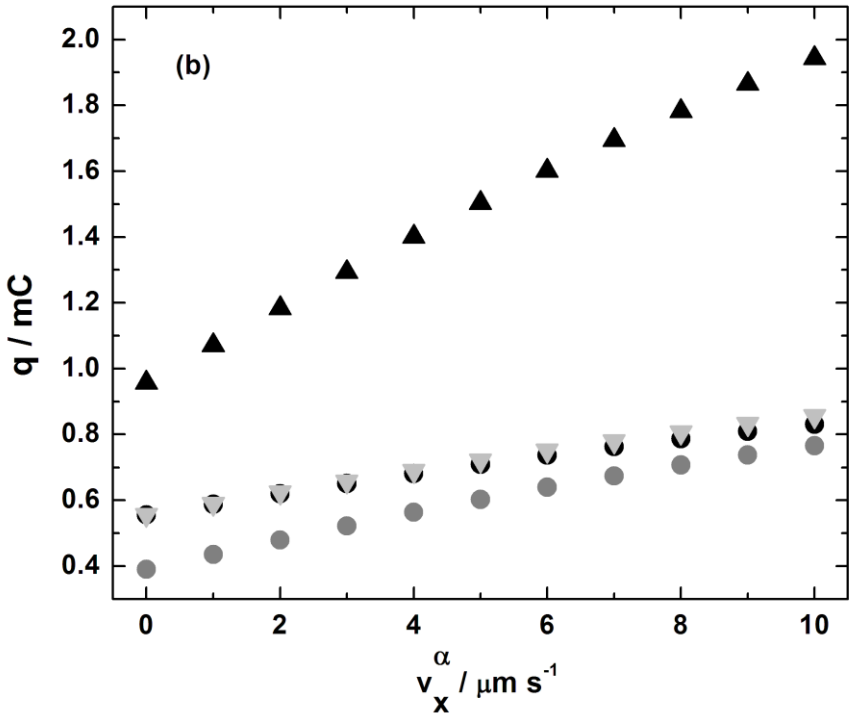


Figure 1b

Figure 1c: Vega Mercado et al.

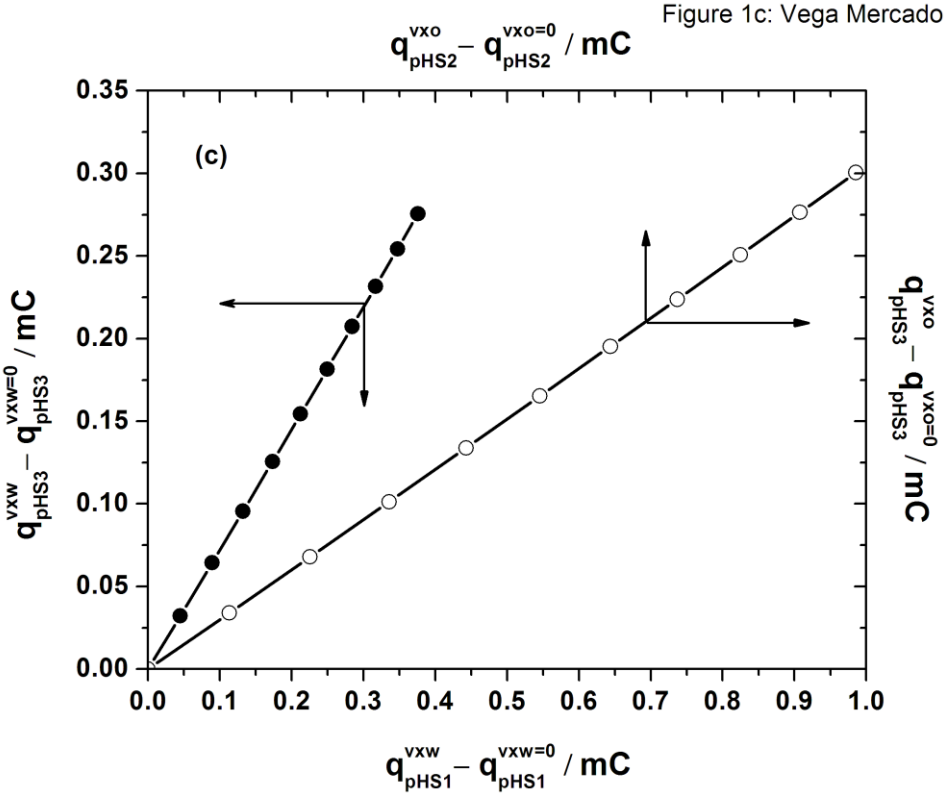


Figure 1c

Figure 2: Vega Mercado et al.

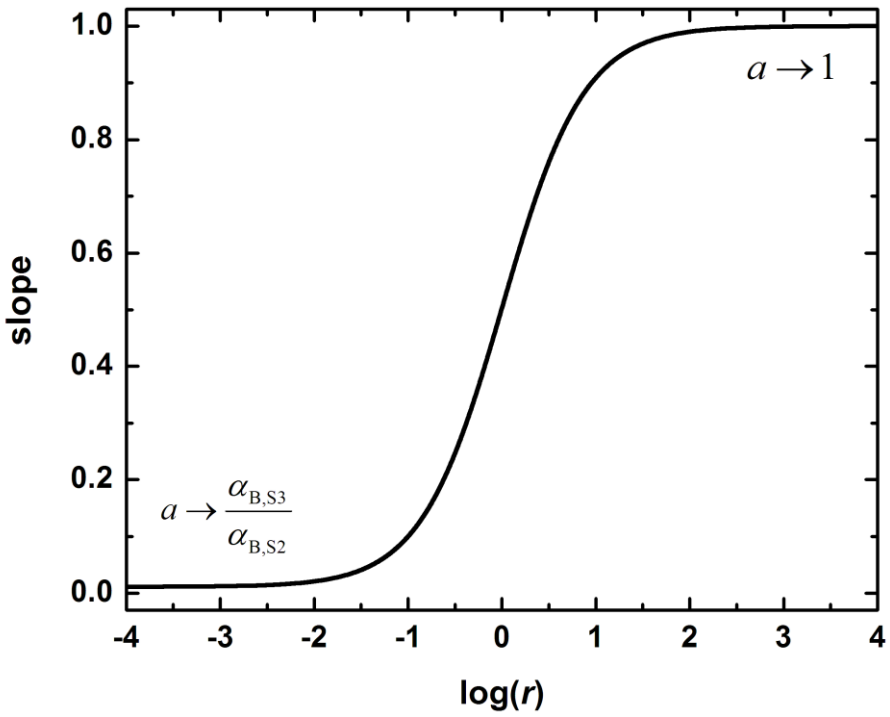

Figure 3: Vega Mercado et al.

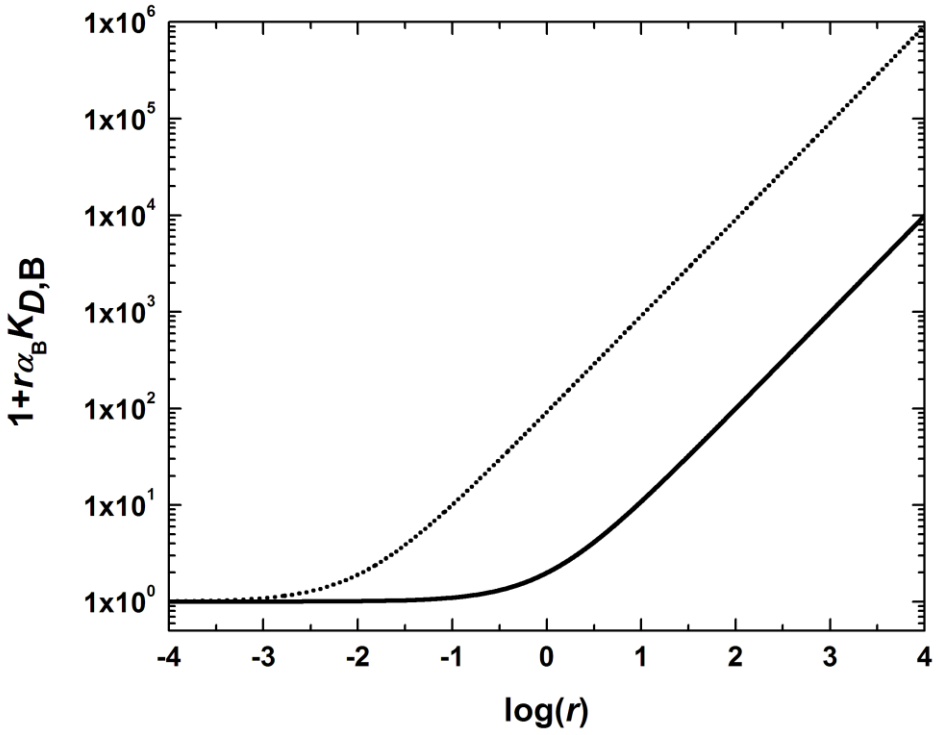

Figure 4: Vega Mercado et al.

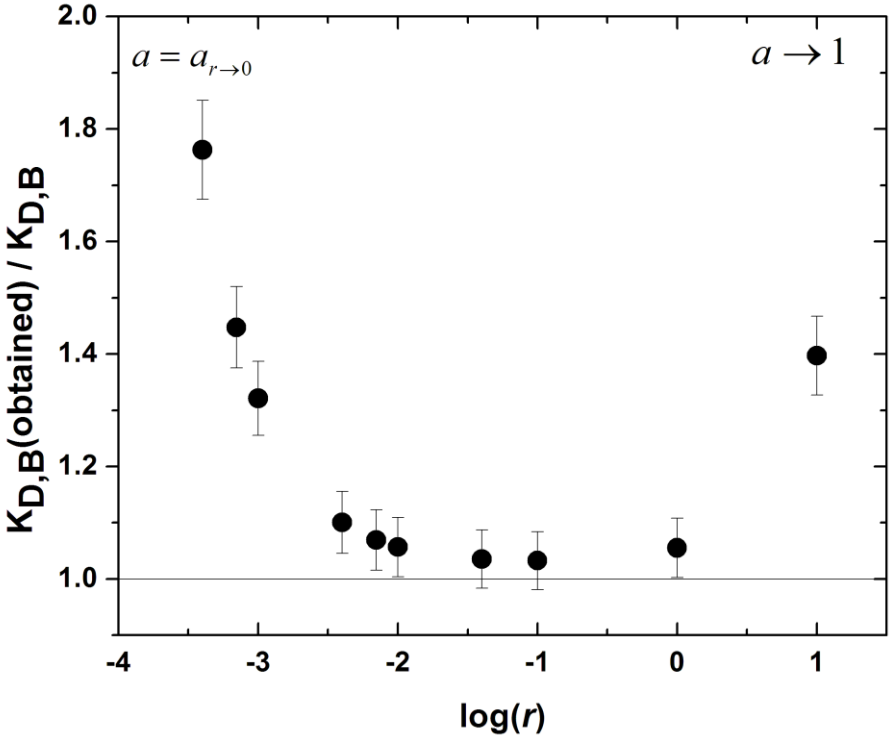

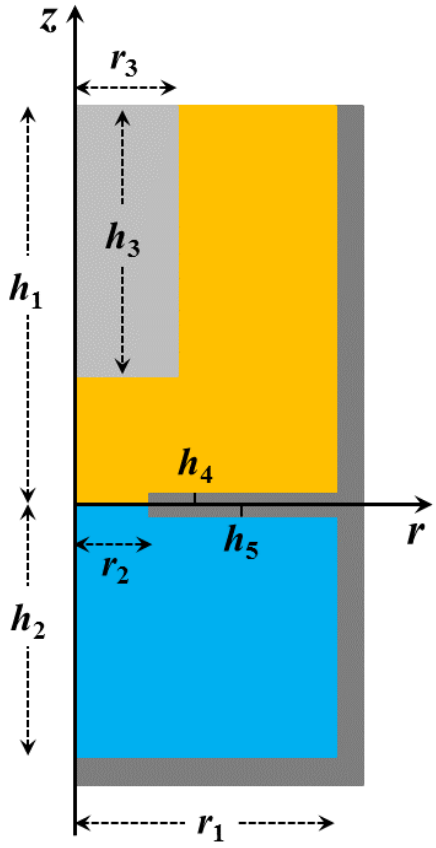


Figure 5: Vega Mercado et al.

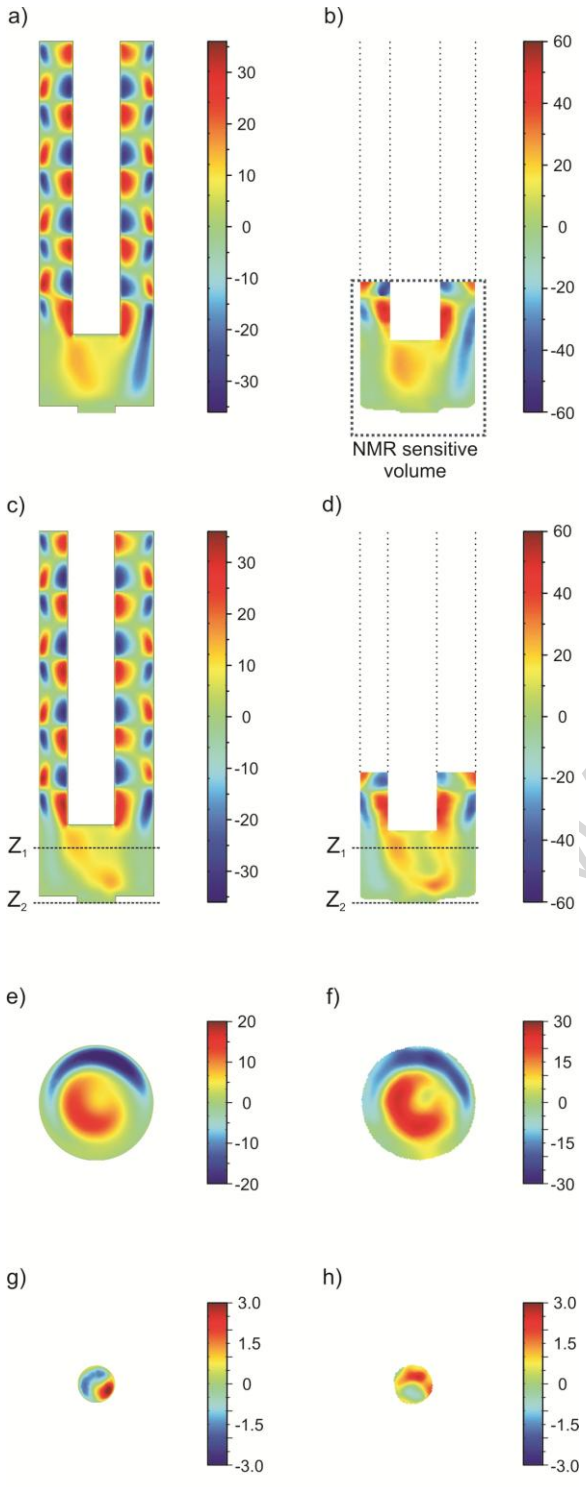


Figure 6

Figure 7: Vega Mercado et al.

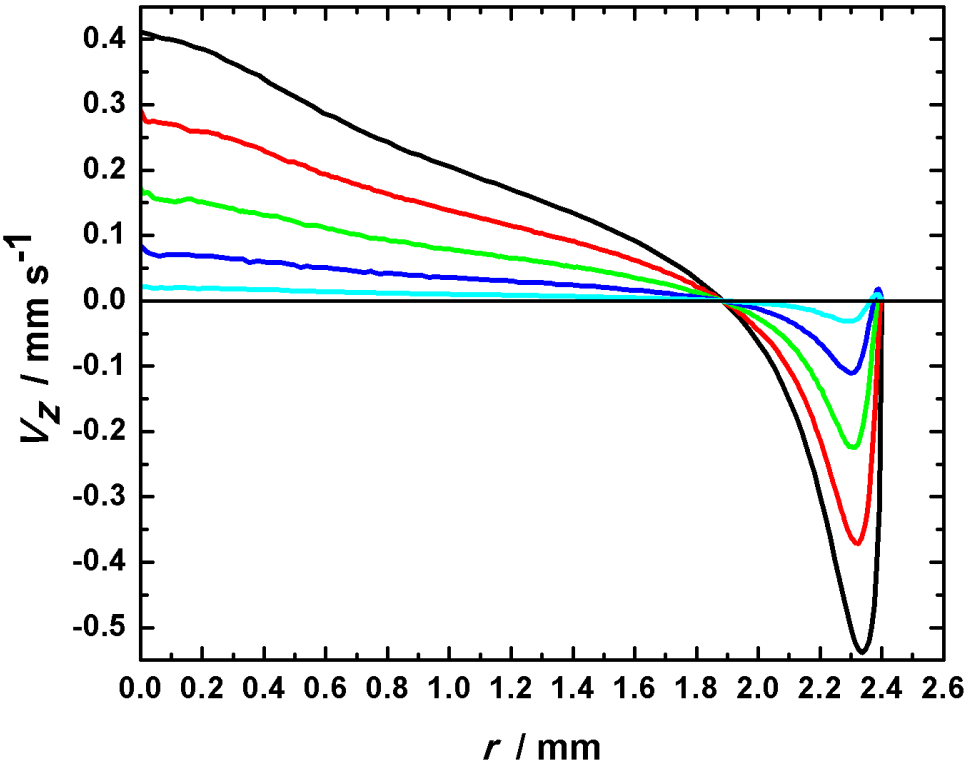

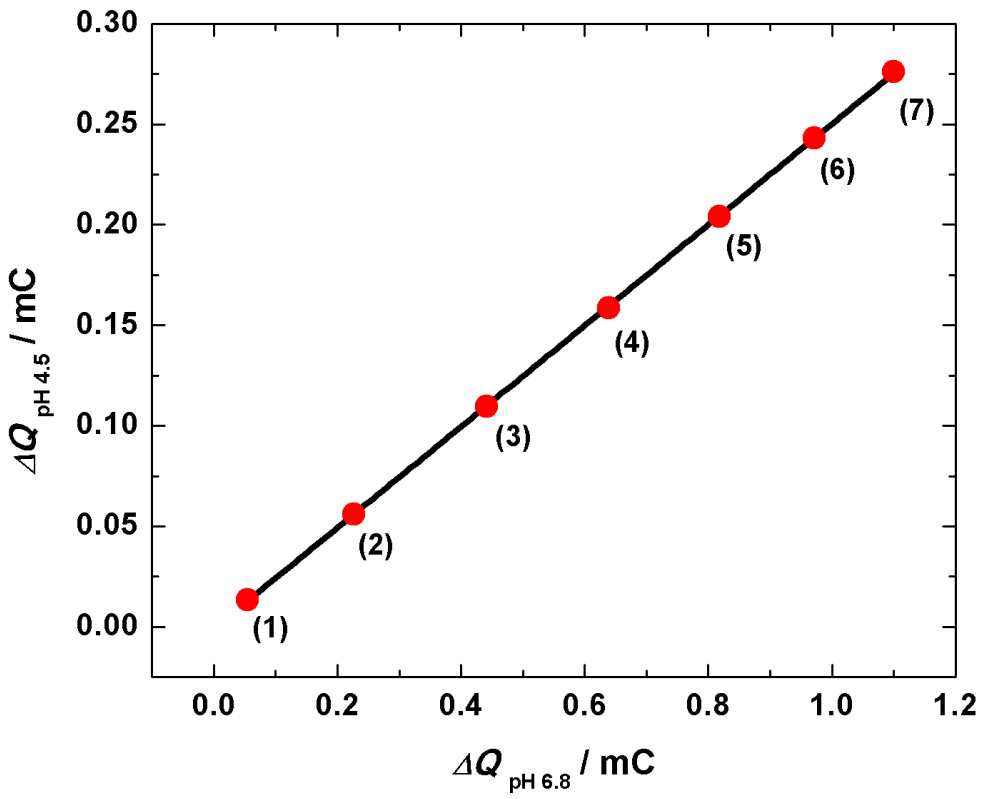


Figure 08 Vega Mercado et al

Figure 8

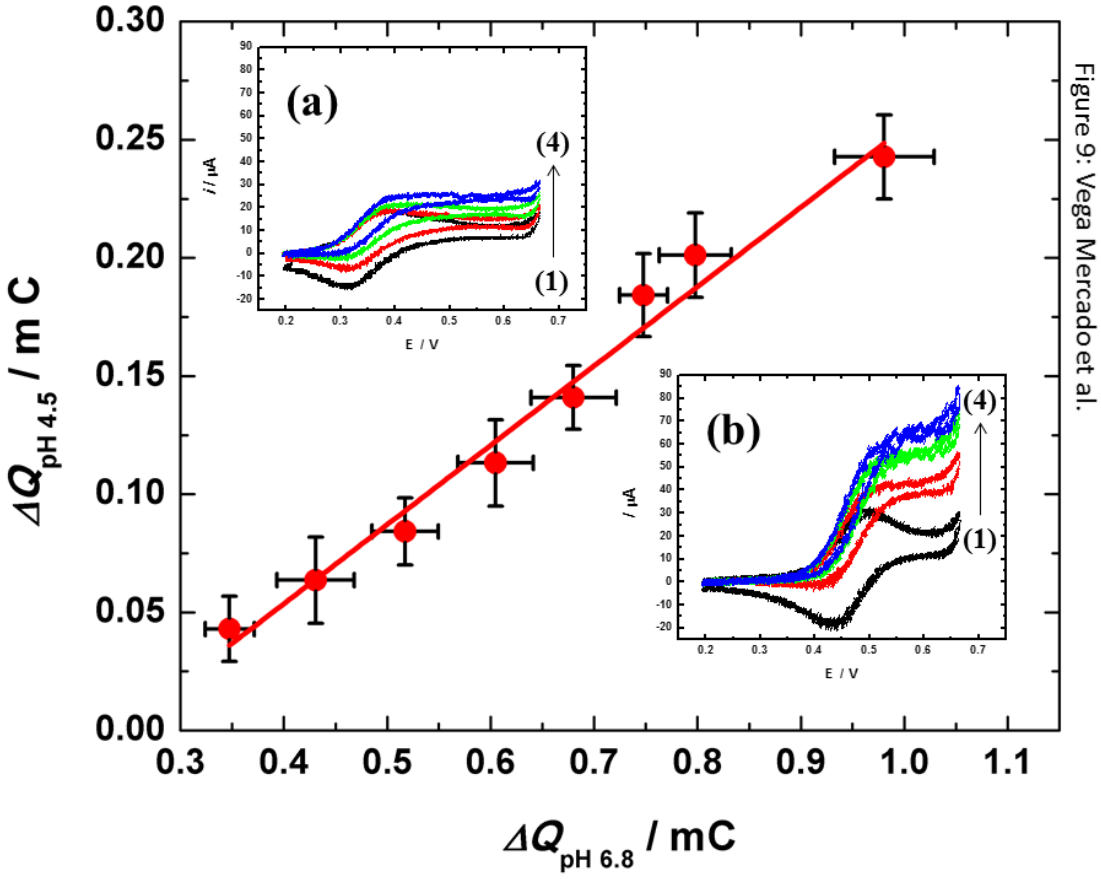


Figure 9: Vega Mercado et al.

Figure 9

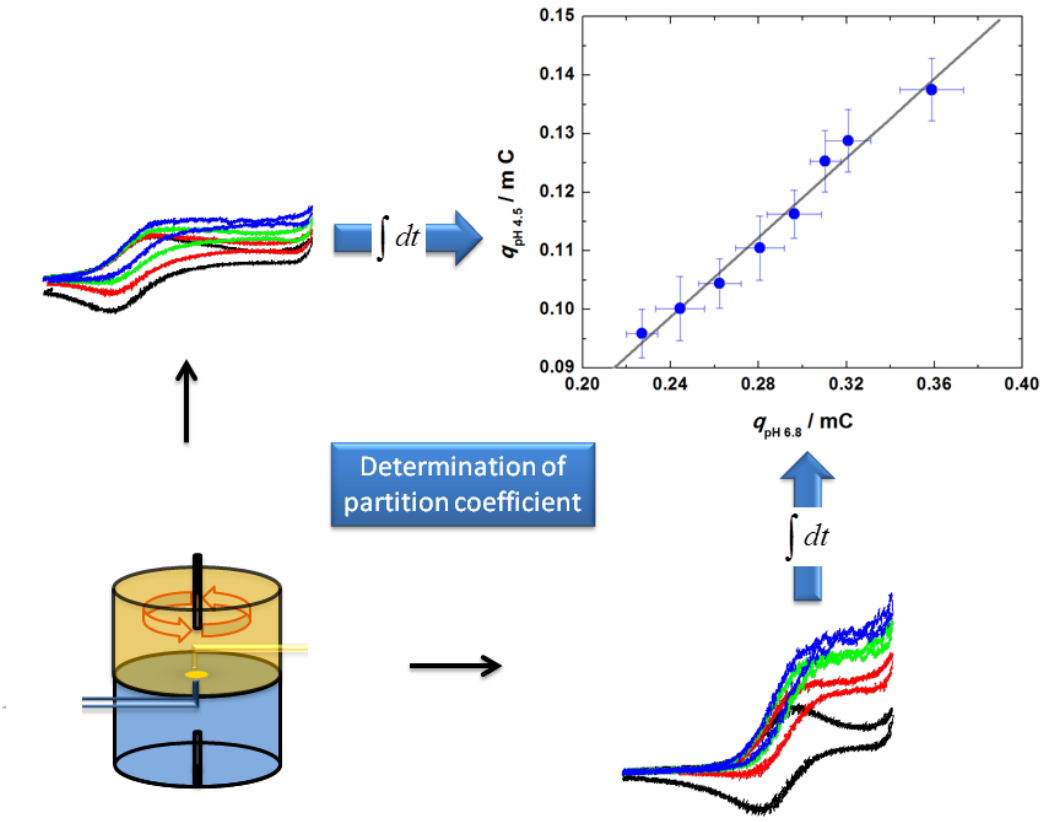


Graphical abstract

**Highlights**

> Comprehensive description of how the forced hydrodynamic conditions affect the facilitated proton transfer

> Methodology for determination of partition coefficients of neutral weak bases is developed

> Novel methodology is experimentally verified.